ROYAL SOCIETY
OF CHEMISTRY

PAPER

Check for updates

Understanding surface chemical processes in perovskite oxide electrodes†

Zijie Sha, Zonghao Shen, [ID] Eleonora Calì, John A. Kilner and Stephen J. Skinner [ID] *

The effect of operating conditions on the surface composition and evolution of $(La_{0.8}Sr_{0.2})_{0.95}Cr_{0.5}Fe_{0.5}O_{3-\delta}$ (LSCrF8255) as a model perovskite oxide was investigated. LSCrF8255 pellets were annealed under dry oxygen ($pO_2 = 200$ mbar), wet oxygen ($pO_2 = 200$ mbar, $pH_2O = 30$ mbar), and water vapour ($pO_2 < 1$ mbar, $pH_2O = 30$ mbar) environments to reflect the applications of perovskite materials as electrodes for oxygen reduction/evolution and H_2O electrolysis in electrochemical energy conversion devices such as solid oxide fuel/electrolysis cells (SOFCs/SOECs) and oxygen transport membranes (OTMs). A series of comprehensive surface characterization techniques were applied, including low energy ion scattering spectroscopy (LEIS), X-ray photoelectron spectroscopy (XPS), secondary ion mass spectrometry (SIMS), scanning electron microscopy (SEM), scanning transmission electron microscopy (STEM), and energy-dispersive X-ray spectroscopy (EDX). Our comprehensive study showed that after annealing at 900 °C for 27 hours, a severe level of Sr surface segregation occurred on the sample annealed in both dry oxygen and water vapour but in different manners, whereas on the sample annealed in wet oxygen, Sr segregation was likely suppressed. In addition, the Sr segregation behaviour can be correlated to other mass transport phenomena, such as Cr evaporation and redeposition and Si deposition, as well as to crystal orientation and defects such as grain boundaries and dislocations. Apart from the Sr-enriched surface precipitates, phase separation was consistently observed on the samples annealed in all three conditions. The secondary phase was found to be B-site cation enriched (significantly Fe enriched, relatively Cr enriched) and A-site cation (La and Sr) deficient. Moreover, in contrast to the Sr enriched surface, a La enriched surface was observed on samples annealed in dry oxygen at 600 and 700 °C, which was found to be potentially caused by the Sr and Cr surface evaporation processes.

1 Introduction

The ability of mixed ionic and electronic conducting (MIEC) perovskite oxides (ABO_3) to support both electronic and ionic conductivity, as well as their desirable catalytic activities and chemical and redox stability under demanding conditions, make them promising electrode materials in electrochemical energy conversion devices ranging from solid oxide fuel/electrolysis cells (SOFCs/SOECs), and oxygen transport membranes (OTMs) to metal–air batteries, as well as in gas conversion and reforming applications.[1–8] In all of these applications, the exchange of oxygen between the gas phase and a MIEC electrode, under elevated temperatures and various oxygen partial pressures, is critical to the overall performance of the device. Since the oxygen exchange process is mediated at the surface of the electrodes, it is not surprising that its kinetics are strongly related to the chemical composition and structure of the surface.[9–15] However, surface instabilities may cause

significant compositional and structural deviations from the bulk. Phenomena such as cation segregation and/or the precipitation of secondary phases are commonly observed on the surface of a range of perovskite oxides under the harsh environments in which they function,[9–11,16–33] having an effect on electrode reactivity and stability.[9–15,34–36] Therefore, it is vital and technologically relevant to develop an in-depth understanding of the nature of the electrode surfaces under their operating conditions and to understand how changes in surface composition influence performance and cause potential degradation in operating devices.

Gas environments have been proven to have a direct impact on the cation surface segregation process on a wide range of perovskite oxides. Taking the commonly reported Sr surface segregation as an example, excess Sr on the surface has been reported in three main phases under different environments: (i) oxides (SrO_x),[11,12,14,16,25–33] (ii) reaction products formed with chemisorbed gases (*e.g.* $Sr(OH)_2$, $SrCO_3$),[17,24,25,27,32,37] and/or (iii) reconstructed Sr-excess phases (*e.g.* $SrCrO_4$).[38] In addition, the extent of cation segregation has been proven to depend on external conditions such as temperature[11,16,17,24] and oxygen partial pressure.[11,39,40] Although the surface composition evolution of MIEC electrodes is widely studied, there has been little

Dept of Materials, Imperial College London, Exhibition Road, London, SW7 2AZ, UK. E-mail: zonghao.shen12@imperial.ac.uk; s.skinner@imperial.ac.uk

This journal is © The Royal Society of Chemistry 2023

J. Mater. Chem. A, 2023, 11, 5645–5659 | **5645**

discussion on the effect of operating conditions on a model system.

In this research, taking $(La_{0.8}Sr_{0.2})_{0.95}Cr_{0.5}Fe_{0.5}O_{3-\delta}$ (LSCrF8255) as a model MIEC perovskite oxide, the surface composition evolution was studied under dry oxygen ($pO_2 = 200$ mbar), wet oxygen ($pO_2 = 200$ mbar, $pH_2O = 30$ mbar), and water vapour ($pO_2 < 1$ mbar, $pH_2O = 30$ mbar) environments, to reflect the implementation of the materials for oxygen reduction/evolution and H_2O electrolysis in the applications mentioned above. It is worth noting that LSCrF8255 was chosen for its excellent bulk stability under both oxidizing and reducing environments at elevated temperatures.[37] The humid environments were of particular interest as water vapour is a fundamental molecule present in the input gas stream of the solid-state electrochemical systems, acting as either impurities beside molecular oxygen in ambient air, or as an electrolysis source for hydrogen production. The surface chemistry and morphology of the materials were investigated using a complementary multi-technique approach. A summary of the low energy ion scattering spectroscopy (LEIS), X-ray photoelectron spectroscopy (XPS), secondary ion mass spectrometry (SIMS), scanning electron microscopy (SEM), scanning transmission electron microscopy (STEM), and energy-dispersive X-ray spectroscopy (EDX) techniques applied in this study is shown in Table 1.

Table 1 highlights the importance of utilizing a combination of different surface characterization techniques as one method is incapable of providing all necessary information. By combining techniques with information depths ranging from the outermost atomic layer (uniquely for LEIS) to the sub- and near-surface region with depth < 10 nm (probed by XPS, angle-resolved XPS, LEIS and SIMS depth profiling, and STEM), to the bulk region with depth in the μm range (probed by SEM and STEM), and the variety of information obtained from each technique, it is demonstrated in this work that a complete and comprehensive understanding of the surface chemistry can be achieved.

2 Results and discussion

2.1. Sr segregated surface chemistry

Cation segregation at the perovskite oxide surface is a commonly observed phenomenon that has a direct impact on the surface reactivity and stability of the material.[9–11,14,16–33]

A-site substituent segregation, especially Sr segregation, is often observed on the surface of perovskite-structured electrode materials in harsh environments.[9–11,14,16–33] The two key driving forces for Sr segregation have been identified as originating from elastic interaction due to the size mismatch between host (La) and substituent (Sr) cations, and electrostatic interaction arising from accumulation of oxygen vacancies ($V_O^{\bullet\bullet}$) in the near surface of MIEC oxides, which results in a positively charged surface with respect to the bulk and further attracts the negatively charged defect (Sr'_{La}) to the surface according to Coulomb's law.[11] In this section, the Sr surface segregation behaviour of LSCrF8255 under the dry oxygen, wet oxygen, and water vapour conditions are first outlined by the quantification results, and then by an in-depth investigation of the surface chemistry focusing on the samples annealed at 900 °C for 27 hours in the three different atmospheres.

2.1.1. Surface chemical states quantification. Fig. 1 and Table S1 in the ESI† present the atomic ratios of $[Sr]_{surface} : [Sr]_{bulk}$ and $[Sr]_{total} : [La]_{total}$ obtained from the LSCrF8255 samples annealed in dry oxygen, wet oxygen, and water vapour conditions at 600, 700, 800, and 900 °C through X-ray photoelectron spectroscopy (XPS) with 0° sample tilt angle and $\approx$ 10 nm probe depth, and angle-resolved XPS (ARXPS) with 80° sample tilt angle and <1 nm probe depth. The quantification of Sr in the bonding environment of surface precipitates $[Sr]_{surface}$, and in the perovskite lattice $[Sr]_{bulk}$, were performed through peak fitting the Sr 3d spectra. An example of the fitted Sr 3d spectrum showing the deconvolution with two sets of spin–orbit split doublets corresponding to two different bonding environments is illustrated in Fig. S3 in the ESI.† The atomic ratio of the total Sr content $[Sr]_{total}$ over the total La content $[La]_{total}$ at sample surfaces was calculated based on the peak areas of the Sr $3d_{5/2}$ and La $3d_{5/2}$ photoelectron peaks after subtraction of a Shirley-type[44] background. All samples were subjected to the same 27 hours of annealing time.

On each sample in Fig. 1a and b, as the probing depth decreases (towards the outermost surface), the atomic ratio of $[Sr]_{surface} : [Sr]_{bulk}$ increases, suggesting a greater amount of Sr surface precipitates can be found closer to the outermost surface. The ratio also increases with annealing temperature under each condition, indicating that the level of Sr at the surface also increases with annealing temperature. In Fig. 1c and d, the atomic ratio of $[Sr]_{total} : [La]_{total}$ was found to be markedly higher than the stochiometric ratio (confirmed on the as-polished sample with

Table 1 Summary of the time-of-flight secondary ion mass spectrometry (ToF-SIMS), low energy ion scattering spectroscopy (LEIS), X-ray photoelectron spectroscopy (XPS), scanning electron microscopy (SEM), scanning transmission electron microscopy (STEM), and energy-dispersive X-ray spectroscopy (EDX) techniques applied in this study.[41–43]

Properties	ToF-SIMS	LEIS	XPS	SEM (imaging, EDX)	STEM (imaging, EDX)
Information depth	1–2 nm	1 atomic layer	1–10 nm	A few nm to tens μm	Sub nm to hundreds nm
Detection limits	ppb	Up to 0.1%	0.1–1%	Up to 0.1%	Up to 0.1%
Lateral resolution	ca. 100 nm–few microns	1–3 μm	ca. 10 μm–1 mm	ca. 1–10 μm	ca. 0.1 nm–1 μm
Elemental information	Yes	Yes	Yes	Yes	Yes
Chemical state information	None	None	Yes	None	None
Quantitative information	Yes (with standards)	Yes	Yes	Yes	Yes
Topography information	None	None	None	Yes	Yes

5646 | *J. Mater. Chem. A*, 2023, **11**, 5645–5659
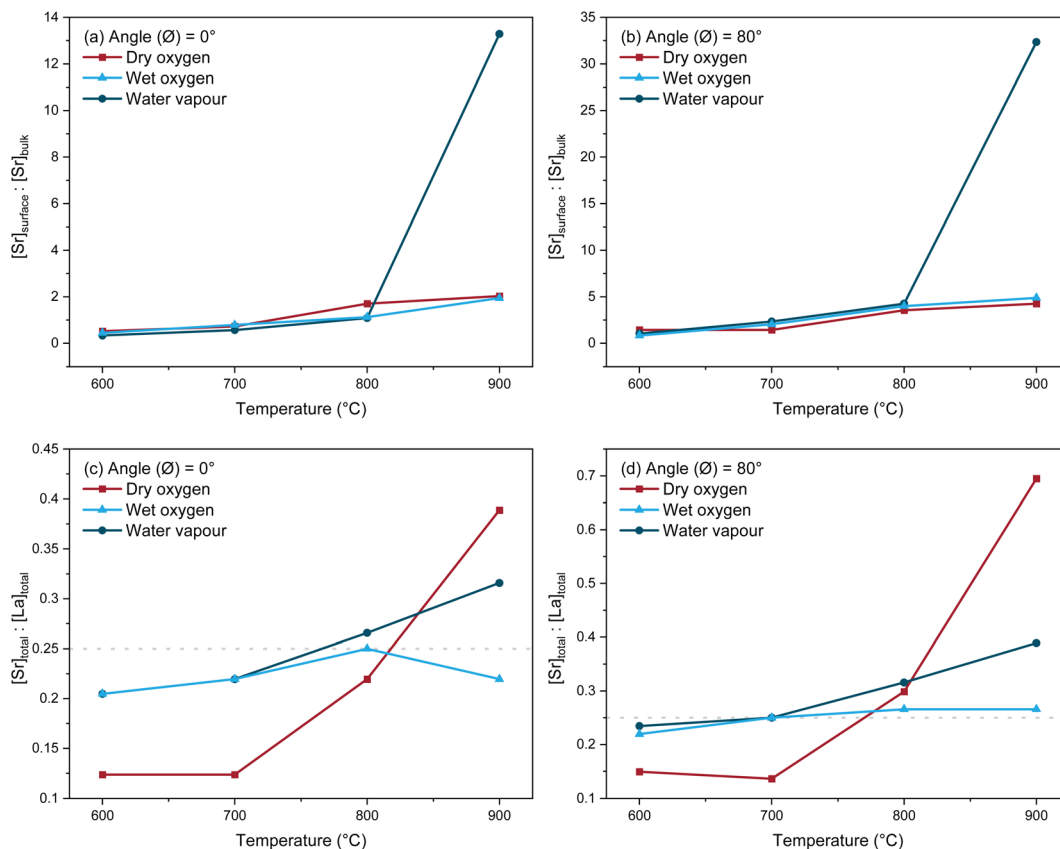
This journal is © The Royal Society of Chemistry 2023

Fig. 1 The $[Sr]_{surface} : [Sr]_{bulk}$ against temperature of the samples annealed in dry oxygen, wet oxygen, and water vapour measured by (a) XPS ($\approx$10 nm probe depth) and (b) ARXPS (<1 nm probe depth); (c and d) the $[Sr]_{total} : [La]_{total}$ against temperature of the same sample measured by (c) XPS and (d) ARXPS. The dashed line indicates the bulk stoichiometry.

data shown in Table S2 in the ESI†) on the surfaces of samples annealed under the dry oxygen and water vapour environments at 900 °C, indicating a severe level of Sr surface segregation and enrichment. On the LSCrF8255 samples annealed at 900 °C, Fig. 1c and d show that the highest ratio of $[Sr]_{total} : [La]_{total}$ was found on the surface of the sample annealed in dry oxygen, followed by the samples annealed in water vapour and wet oxygen. However, the sample annealed in water vapour showed the highest $[Sr]_{surface} : [Sr]_{bulk}$ fraction. In addition, in contrast to the other two annealing conditions, no obvious Sr surface enrichment was detected on the surface of the sample annealed in wet oxygen.

Low energy ion scattering (LEIS) depth profiling was further applied to confirm the relative trend in $[Sr]_{total} : [La]_{total}$ in the samples annealed at 900 °C in dry oxygen, wet oxygen, and water vapour conditions. The LEIS spectra collected from the annealed samples, alongside an as-polished sample, are illustrated in Fig. 2. In Fig. 2, as compared to the as-polished sample, the outermost surfaces of all the annealed samples are enriched in A-site cations with clearly visible peaks corresponding to La and Sr. After light sputtering, the signal for the respective transition metal cations (Cr and Fe) can be observed clearly in the layers beneath the surface. These observations are in good agreement with LEIS results previously reported for as-polished and heat-treated LSCrF and $La_{0.6}Sr_{0.4}Co_{0.2}Fe_{0.8}O_{3-\delta}$ (LSCF) samples.[18,45]

The LEIS depth profiles of the ratio of A-site cations $[Sr]_{total} :$ $[La]_{total}$, the ratio of total A-site cation content over total B-site cation content $([Sr] + [La]) : ([Cr] + [Fe])$, and the ratio of B-site cations $[Cr]_{total} : [Fe]_{total}$ for the as-polished and annealed LSCrF8255 samples are illustrated in Fig. 3.

The depth profiles in Fig. 3a show clear evidence of Sr segregation towards the surface in all samples. Sr enrichment in the as-polished sample could be due to small-scale reorganisation of the surface cations caused by potential mechanical damage from polishing. Compared to the as-polished sample, the extent of Sr surface enrichment was significantly greater on the samples annealed at 900 °C. This trend in Sr enrichment is in good agreement with the XPS results displayed in Fig. 1c and d, confirming that the Sr surface enrichment level was highest on the sample annealed in dry oxygen, with the highest $[Sr]_{total} :$ $[La]_{total}$ ratio up to Ar^+ fluences of 30×10^{15} cm^{-2} (estimated depth $\sim$6 nm), followed by the samples annealed in water vapour and wet oxygen. It is worth noting that two different sets of samples with the same thermal history were used for the XPS and LEIS analysis.

The significant difference in Sr enrichment under the different atmospheres could be mainly the result of the combined effect of oxygen partial pressure difference and humidity. Due to the difference in the oxygen partial pressure in the dry oxygen ($pO_2 = 200$ mbar) and water vapour ($pO_2 < 1$
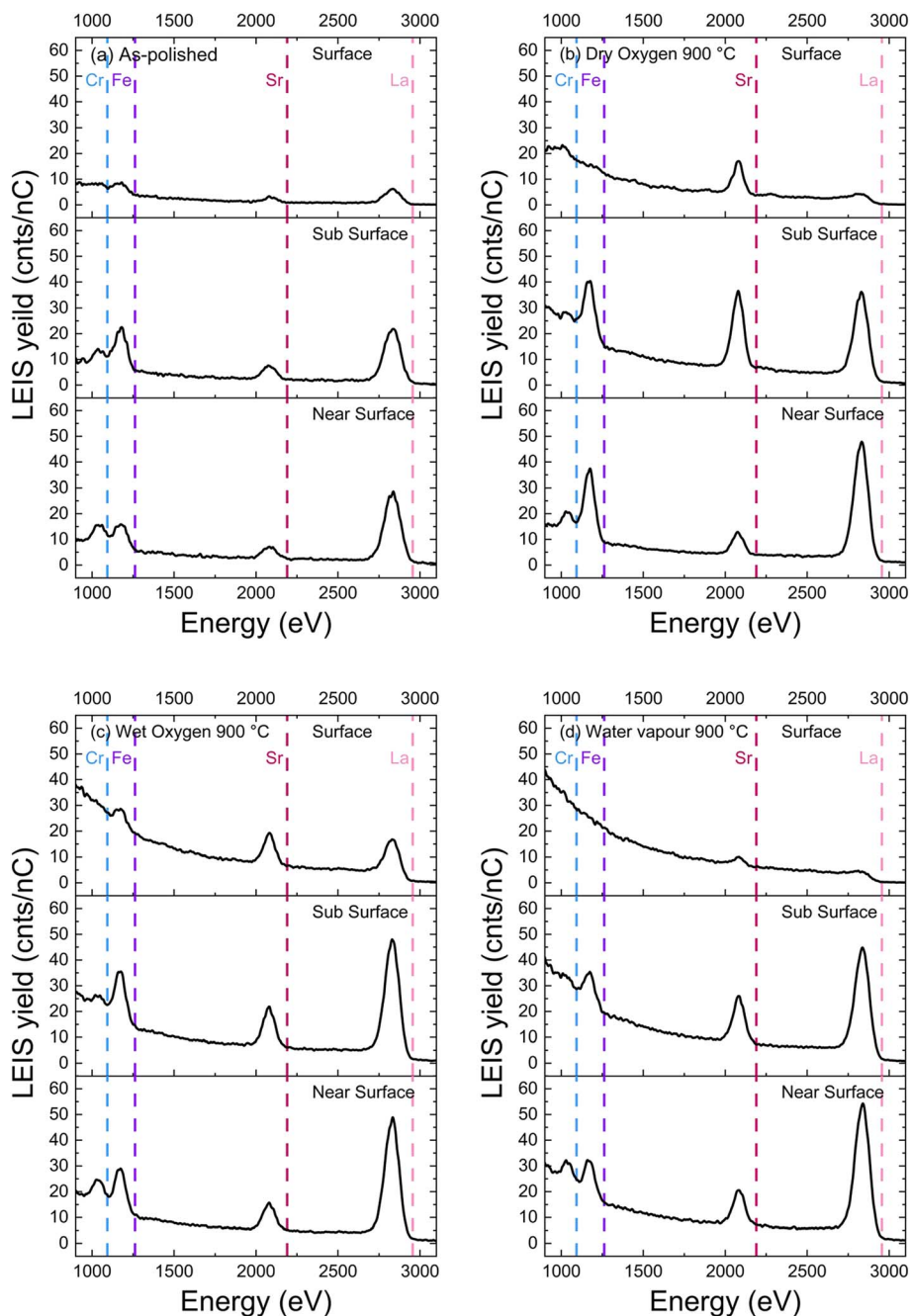
Fig. 2 (a–d) The $^{20}Ne^+$ (5 keV) LEIS spectra of the (a) as-polished LSCrF8255 samples, and the samples annealed at 900 °C for 27 hours in (b) dry oxygen, (c) wet oxygen, and (d) water vapour conditions. The top spectra were obtained from the immediate outermost surfaces, the middle spectra are from sub-surfaces after removal of a small amount of material by Ar^+ sputtering of approximately 4.6×10^{15} cm^{-2}, and the bottom spectra represent the near surfaces after sputtering up to a fluence $>25 \times 10^{15}$ cm^{-2}.

mbar, $pH_2O = 30$ mbar), different amounts of oxygen vacancies were found on the annealed samples with the same thermal history.[37] Since the electrostatic interaction, between the positively charged oxygen vacancies ($V_O^{\bullet\bullet}$) in the near surface and the negatively charged defect (Sr'_{La}), is one of the key driving forces for Sr surface segregation, distinct Sr enrichment levels were observed. In addition, studies have shown the effect of washing surfaces of perovskite oxides with water could reduce Sr-rich surface species.[30,46] Further,

correlating with the previous studies in oxygen transport properties in the same three conditions, it has been found that despite the Sr segregation being limited in the wet oxygen atmosphere, the surface exchange kinetics were also limited due to the competition between water molecule and molecular oxygen for the surface oxygen vacancy sites, as well as the molecular scrambling between the two species.[24,47] In comparison to the significantly enhanced (up to 4 orders of magnitude) oxygen transport properties in the water vapour as
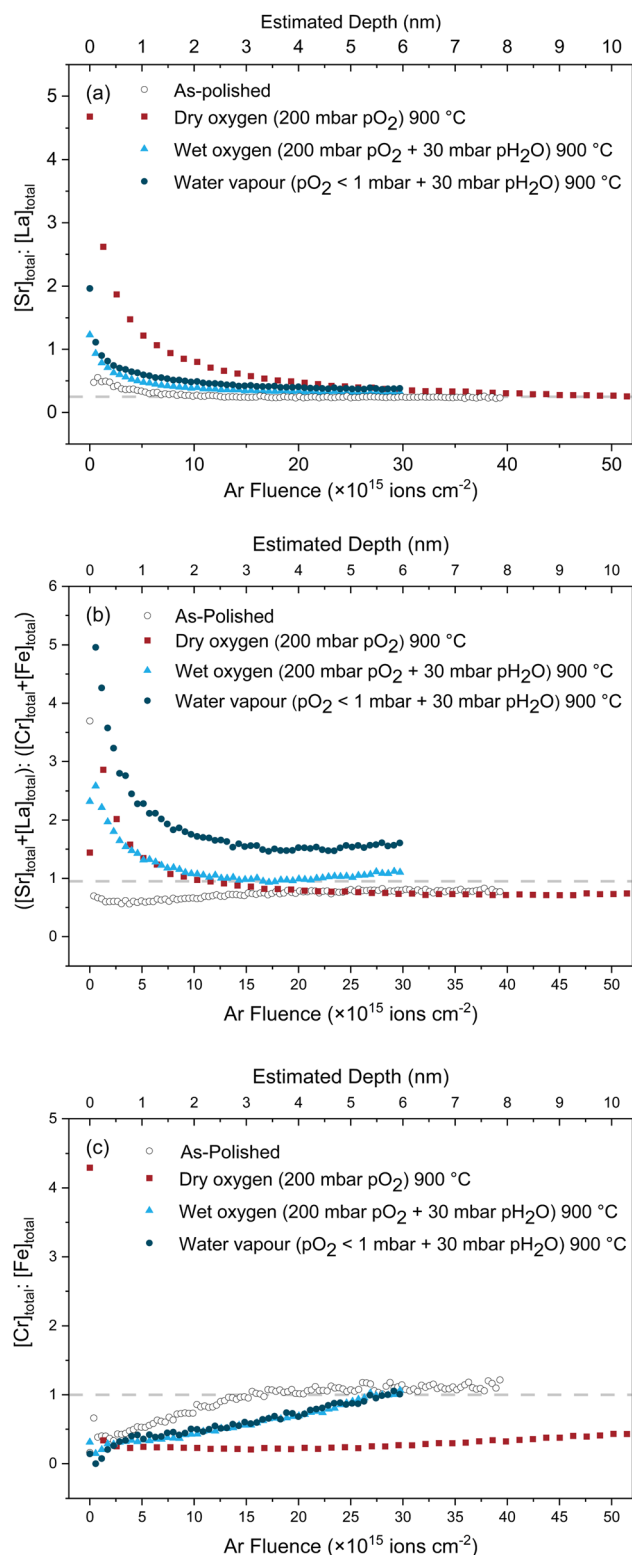
5648 | *J. Mater. Chem. A*, 2023, **11**, 5645–5659

This journal is © The Royal Society of Chemistry 2023

Fig. 3 LEIS depth profiles showing the atomic ratio of (a) $[Sr]_{total}$: $[La]_{total}$, (b) $([Sr] + [La])$: $([Cr] + [Fe])$, and (c) $[Cr]_{total}$: $[Fe]_{total}$ for the as-polished sample, and the samples annealed at 900 °C for 27 hours in dry oxygen, wet oxygen, and water vapour conditions. The dashed line indicates the nominal bulk stoichiometry.

compared to the other two conditions,[37] the extent of Sr surface enrichment was moderate.

In Fig. 3b, the as-polished sample shows an A-site cation enriched outermost surface followed by B-site cation enriched subsurface layers. The subsurface layers are particularly enriched in Fe, as indicated in Fig. 3c. The enrichment in Fe at the B-site in the subsurface region was also reported by Wong[45] for an as-polished LSCrF8255 sample, and by Niania *et al.*[48] for an as-polished LSCF sample. In contrast, Fig. 3b shows AO-dominated top surface layers on all the annealed samples. The sample annealed in water vapour shows the highest degree of A-site cation enrichment, although the sample annealed in dry oxygen shows the highest Sr enrichment, Fig. 3a. This observation suggests that there are different surface reconstruction mechanisms and the different chemical compositions of the surface Sr species under the different annealing conditions, which will be discussed in Section 2.1.2 below. Further, Fig. 3c shows that, except for the significantly Cr-enriched outermost surface found with the dry oxygen annealed sample, Fe enrichment or Cr depletion is observed in the immediate sublayers of all the annealed samples and the extent of the Fe enrichment is greater than that of the as-polished sample up to Ar$^+$ fluences of 30×10^{15} cm^{-2} (estimated depth $\sim$6 nm). The shape of the depth profile of $[Cr]_{total}$: $[Fe]_{total}$ is similar for the samples annealed in wet oxygen and water vapour. The depths of the Fe-enriched subsurface layers of the two samples annealed in humid atmospheres are shorter than that of the sample annealed in dry oxygen. Table S3 in the ESI† displays the atomic ratio of $[Cr]_{total}$: $[Fe]_{total}$ collected from the as-polished sample and the annealed samples through XPS and ARXPS. The ratio was calculated based on the peak areas of the Cr 2p$_{3/2}$ and Fe 2p$_{3/2}$ photoelectron peaks after subtraction of a Shirley-type[44] background. In Table S3,† no Fe enrichment can be observed on the samples annealed in wet oxygen and water vapour. By contrast, the as-polished sample and the sample annealed in dry oxygen show a relatively Fe-enriched near surface layer compared to the outer surface layers, although the differences are insignificant and within the quantification uncertainty of XPS analysis.[49]

2.1.2. Segregated surface composition and phase separation. A detailed assessment of the surface composition of the samples annealed under different environments is essential in order to understand the quantification results. In this section, the chemical bonding environment of each constituent ion in LSCrF8255, the surface chemical composition, the surface morphology, and the chemical composition of the secondary phase were analysed through XPS, STEM-EDX, SEM, and SEM-EDX, respectively.

2.1.2.1 Bonding environment of the surface cations. A comparison of the La 3d$_{5/2}$, Sr 3d, Cr 2p and Fe 2p spectra collected from the samples annealed in the three different conditions at 900 °C for 27 hours are displayed in Fig. 4.

In Fig. 4a, the spin–orbit component, La 3d$_{5/2}$, is split by multiplet splitting due to charge transfer from the ligand O 2p valence band to the La 4f.[50,51] The La chemical bonding environment can be determined through the magnitude of the multiplet splitting and the intensity ratio of each multiplet split
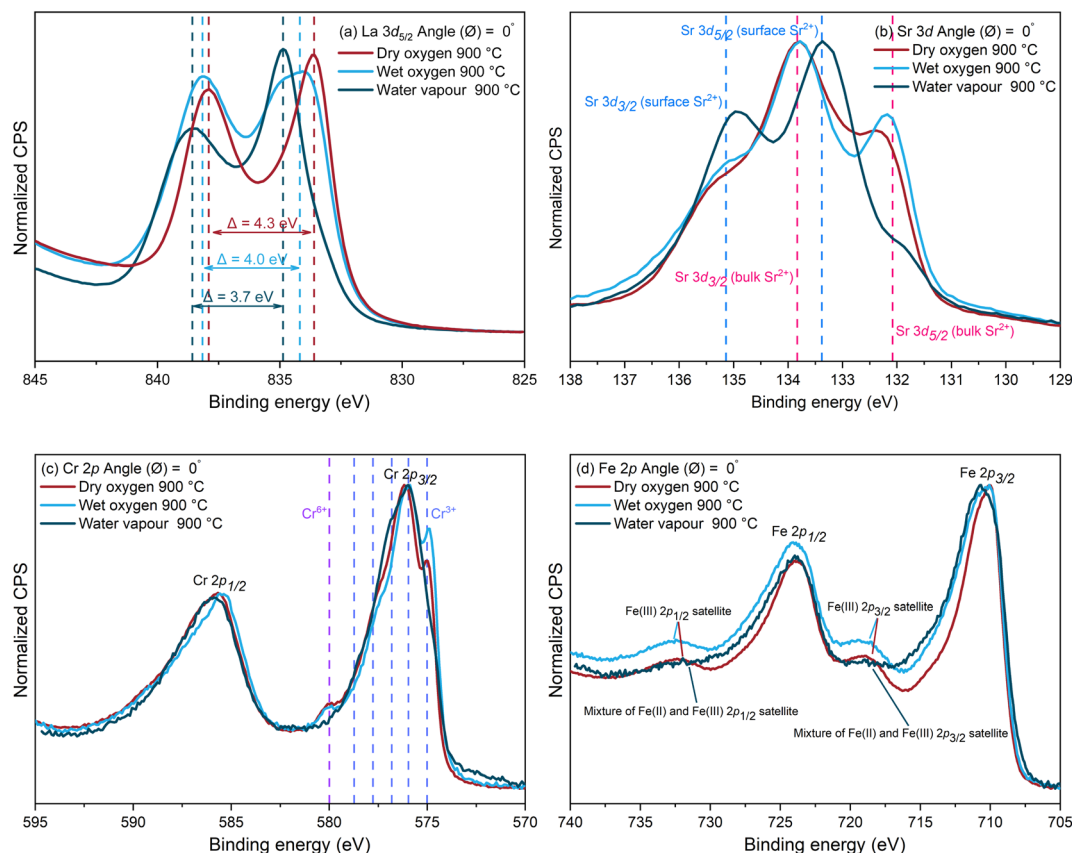
This journal is © The Royal Society of Chemistry 2023

J. Mater. Chem. A, 2023, **11**, 5645–5659 | **5649**

Fig. 4 The (a) La 3d$_{5/2}$, (b) Sr 3d, (c) Cr 2p, and (d) Fe 2p XPS spectra of the samples annealed in dry oxygen, wet oxygen, and water vapour at 900 °C for 27 hours.

component.[50–52] The peak separation and the satellite-to-main-peak intensity ratio are both higher for La$_2$O$_3$ than for La(OH)$_3$.[50] This is due to the larger covalency of La–O bonds, as well as stronger hybridisation between the 4f orbital and the valence band in the final state for the oxide compared to the hydroxide.[50,51] The peak separation is found to be 4.3 eV for the sample annealed in dry oxygen, in good agreement with values reported in literature for La$_2$O$_3$ and lanthanum transition metal perovskite oxides.[51–55] This further suggests that the La surface species is most likely to be La$_2$O$_3$. A relatively smaller peak separation (3.7 eV) was observed with the sample annealed in water vapour, suggesting that La(OH)$_3$ is potentially the dominant La surface species, with a value of 3.9 eV reported in literature.[50] In addition, the satellite-to-main-peak intensity ratio was found to be approximately 0.72 for the sample annealed in water vapour, smaller than that of 0.88 found on the sample annealed in dry oxygen. For the sample annealed in wet oxygen, the peak separation was found to be 4.0 eV, suggesting there was likely a mixture of La$_2$O$_3$ and La(OH)$_3$ on the sample surface. For all three samples, the La surface species was very unlikely to be La$_2$(CO$_3$)$_3$ as the carbonate signal is not detectable on the C 1s spectra displayed in Fig. S4 in ESI.†

The Sr 3d spectra in Fig. 4b show the deconvolution with two sets of spin–orbit split doublets, with one at higher binding energy arising from the [Sr]$_{surface}$ and the other at lower binding energy attributed to [Sr]$_{bulk}$. The [Sr]$_{surface}$ signal was found to be particularly high on the sample annealed in water vapour. The quantification results of [Sr]$_{surface}$: [Sr]$_{bulk}$ are displayed in Fig. 1 and Table S1.† The Sr-based surface precipitates formed in the humid atmospheres are more likely to be Sr(OH)$_2$ considering the lack of carbonate bond signature in the C 1s spectra, displayed in Fig. S4 in the ESI,† and the strong hydroxyl bond signature shown in the O 1s spectra, displayed in Fig. S5 in the ESI.† The formation of the Sr(OH)$_2$ could be due to the reaction of water molecules with SrO formed on the top surface layers:

$$SrO_{(surf)} + H_2O_{(g)} = Sr(OH)_{2(surf)} \tag{1}$$

This finding is supported by a theoretical study by Staykov *et al.*[32] on the interaction of water in the gas phase with a SrO-terminated surface of a 2,4-perovskite oxide, SrTiO$_3$. For the sample annealed in dry oxygen, the Sr-based surface precipitates are more likely to be SrO$_x$.[11,12,14,16,25–33,56] More details regarding the chemical composition of the surface precipitates are revealed by STEM-EDX in the Section 2.1.2.2 below.

The Cr 2p spectra in Fig. 4c show two distinct spin–orbit components, Cr 2p$_{3/2}$ and Cr 2p$_{1/2}$. Multiplet splitting can also be observed, which is due to the interaction between the core electron vacancy created by X-ray irradiation in the 2p shell and the three unpaired 3d electrons of Cr^{3+} (3d t$_{2g}^3$), creating a number of final states.[57] Only the Cr 2p$_{3/2}$ component is fitted

5650 | *J. Mater. Chem. A*, 2023, **11**, 5645–5659

This journal is © The Royal Society of Chemistry 2023

with six peaks attributed to multiplet splitting, due to the complexity of the Cr 2p$_{1/2}$ component arising from Auger signals and satellite features.[58–60] An example of the fitted Cr 2p spectrum is illustrated in Fig. S6 in the ESI.† The peaks attributed to Cr^{3+} are in accordance with the binding energies reported for Cr$_2$O$_3$.[57–60] The existence of Cr in a higher oxidation state, Cr^{6+}, on the samples annealed in dry and wet oxygen with high pO$_2$, is confirmed by the peak at approximately 580 eV and in good agreement with the binding energies reported for CrO$_3$ and La$_{0.8}$Sr$_{0.2}$CrO$_3$.[38,55,59,60] There is a single peak arising for Cr^{6+} due to no unpaired electrons in its outermost shell. On the contrary, the Cr^{6+} signal can scarcely be observed on the sample annealed in the water vapour environment with low pO$_2$. Fig. S7 in the ESI† illustrates the Cr 2p spectra of the as-polished samples and samples annealed in water vapour at 600–900 °C. No Cr^{6+} species were detected on either of these samples. This result suggests that the oxidation of Cr is only likely to occur during annealing in oxidizing environments. This phenomenon can be further correlated with the Sr surface segregation and will be discussed in Section 2.1.2.2 and 2.2.

In Fig. 4d, due to complex multiplet splitting and satellite features associated with high-spin Fe compounds,[60–62] as well as the many possible species with overlapping binding energies, peak fitting of the Fe 2p spectra is extremely difficult and may result in erroneous interpretation.[60] Nevertheless, the satellite features suggest the oxidation state of Fe is "+3" on the samples annealed in dry and wet oxygen, and the valence state of Fe is reduced on the sample annealed in water vapour, with a mixture of Fe^{2+} and Fe^{3+} species present on the surface.[60–62] The Fe 2p spectra of the as-polished sample and samples annealed in water vapour at 600–900 °C are illustrated in Fig. S8 in the ESI.† A change in the shape of the satellite features can also be observed on the samples annealed in water vapour at various temperatures compared to the as-polished sample, suggesting the reduction in the Fe oxidation state. It is worth noting that

the reduction in the valence state of the B-site cations can provide an indication of the state of oxygen vacancies, since the reduction could be charge compensated by accommodating a larger number of vacancies on the surface of the perovskite structure. This can be further correlated to the significantly enhanced oxygen transport properties, by up to 4 orders of magnitude, of the LSCrF8255 samples annealed in water vapour reported in our previous study.[37]

2.1.2.2 Surface composition characterized by STEM-EDX. An energy-dispersive X-ray spectroscopy elementary map carried out in the scanning transmission electron microscope mode (STEM-EDX) was obtained from the sample annealed in dry oxygen at 900 °C for 27 hours to further study the chemical environment of Sr surface species, illustrated in Fig. 5.

In Fig. 5, the top surface layer of the sample was found to be relatively Sr- and Cr-enriched, suggesting the formation of a SrCrO$_4$-like compound. SrCrO$_4$ formation has been reported in several previous studies of lanthanum strontium-based perovskite oxides applied as electrodes, mainly due to Cr deposition from the Fe–Cr interconnect of solid oxide fuel cells (SOFCs) towards the SrO covered surface.[63–69] In this case, the SrCrO$_4$ is likely formed through the oxidation of Cr species on the sample surface to volatile Cr^{6+} species such as CrO$_3$.[38] The Cr^{6+} gaseous species would further react with the segregated SrO particles on the surface to form SrCrO$_4$-like oxides:[63–66]

$$CrO_{3(g)} + SrO_{(surf)} \rightarrow SrCrO_{4(surf)} \quad (2)$$

The nucleation theory proposed by Jiang *et al.*[65] suggests selective and preferential Cr deposition on the segregated SrO on the surface, which acts as the nucleation agent. The reaction between the SrO and gaseous Cr species would further result in the formation, growth, and crystallization of SrCrO$_4$. The Cr evaporation and redeposition theory is further supported by the XPS results. Fig. S9 in the ESI† illustrates a comparison of the Cr
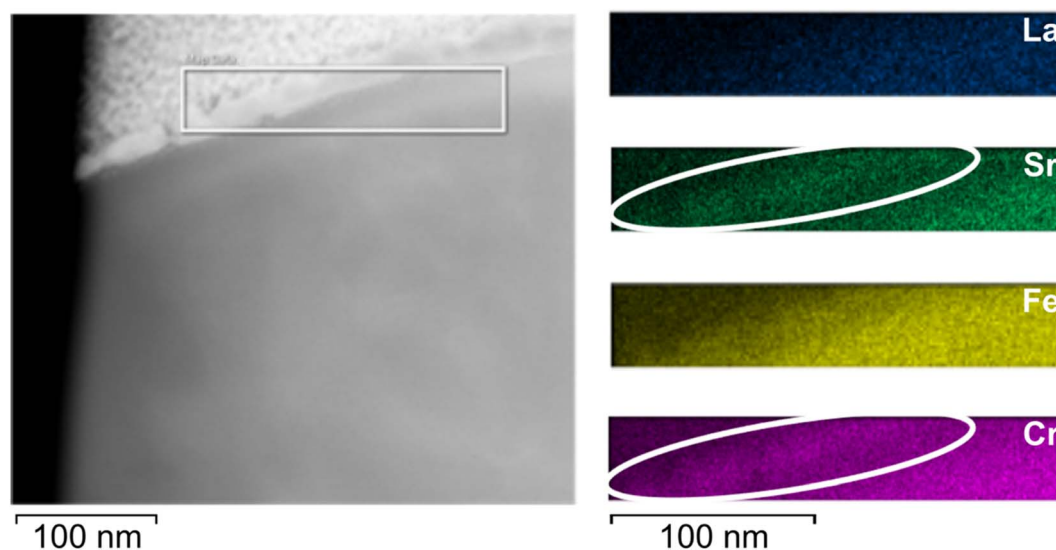

Fig. 5 STEM-EDX map focusing on the surface region of the sample annealed in dry oxygen at 900 °C for 27 hours highlighting the Sr- and Cr-enriched top surface layer.

This journal is © The Royal Society of Chemistry 2023

J. Mater. Chem. A, 2023, **11**, 5645–5659 | **5651**

2p spectra collected through XPS (≈ 10 nm probe depth) and ARXPS (<1 nm probe depth) from the sample annealed in dry oxygen at 900 °C for 27 hours. The atomic ratios of $[Cr^{6+}]:[Cr^{3+}]$ and $[Cr]_{total}:[Fe]_{total}$ obtained from the sample are displayed in Table S4 in the ESI.† Fig. S9 and Table S4† show that the amount of Cr^{6+} species and total Cr content are marginally higher closer to the outermost surface layer. In addition, the Cr oxidation and evaporation during the heat treatment in oxidizing conditions (static air, dry and wet oxygen) could be one of the potential reasons for the Fe enriched surface layers observed in LEIS (Fig. 2 and 3). Further, no evidence of a Cr-enriched surface was detected on the sample annealed in wet oxygen at 900 °C for 27 hours.[24] It is likely that the Cr evaporation and redeposition is suppressed by the presence of water vapour in the atmosphere.

In our previous studies, Si deposition was observed on the LSCrF8255 samples annealed in both the wet oxygen and water vapour conditions in STEM-EDX and XPS analysis.[24,37] In contrast, there was no Si detectable on the samples annealed in dry oxygen. The Si deposition likely results from the transport of volatile Si species in the wet atmospheres, which were formed due to the reaction between water molecules and the quartz glass tube used for the annealing.[13] An example of a STEM-EDX map showing Si deposition obtained from the sample annealed in water vapour at 900 °C for 27 hours is illustrated in Fig. 6.

In Fig. 6, the top surface layer of the sample is Sr- and Si-enriched, suggesting the formation of a reconstructed $SrSiO_3$-like phase, which could be due to the reaction between the Sr surface species with the deposited Si species. A B-site cation enriched (Fe and Cr enriched) and A-site cation (La and Sr) deficient secondary phase can also be identified. The formation of the secondary phase under the different atmospheres will be discussed in Section 2.1.2.3 below. Additionally, Table S5 in the ESI† compares the extent of Si deposition on the surfaces of the samples annealed in humid atmospheres at 900 °C for 27 hours. It indicates that the amount of $[Si]_{total}$ deposited on the sample annealed in water vapour was approximately 13 at.% greater than that deposited on the sample annealed in wet oxygen.

2.1.2.3 Surface morphology and phase separation. A different surface morphology can be observed on the samples annealed in dry oxygen, wet oxygen and water vapour. Fig. 7 illustrates the secondary electron (SE) images obtained from the as-sintered samples and samples annealed in the three conditions at 900 °C for 27 hours through scanning electron microscopy (SEM).

In Fig. 7, compared to the as-sintered sample (Fig. 7a), the SE images of the annealed samples (Fig. 7b–d) display the varied morphologies of a thermally etched surface. There are several interesting observations worth noting. First, on the samples annealed in wet oxygen (Fig. 7c) and water vapour (Fig. 7d) conditions, there was coarsening of the particles, particularly along the grain boundaries. This suggests that the grain boundaries could be the preferable site for nucleation and agglomeration of Sr-enriched precipitates in humid atmospheres. By contrast, no grain boundary precipitates were observed on the sample annealed in dry oxygen (Fig. 7b). Second, external defects which have been induced by grinding or polishing affect the growth of surface particles. It can be observed that precipitates formed along scratches on the samples annealed in water vapour (Fig. 7d), and possibly in dry oxygen (Fig. 7b). This phenomenon may be due to enhanced segregation within the dislocation network formed due to mechanical damage and/or the damaged surfaces acting as heterogeneous nucleation sites for the precipitates.[17] In addition, for all three annealed samples, the precipitation behaviour varied both quantitatively and dimensionally between grains. In Fig. 7b–d, as indicated by the black circles, there are some grains which accommodate a large number of precipitates on their surface, while other grains show a more limited number of precipitates. This grain-dependent precipitation behaviour suggests that Sr segregation could be affected by crystal orientation, in accordance with previous findings on
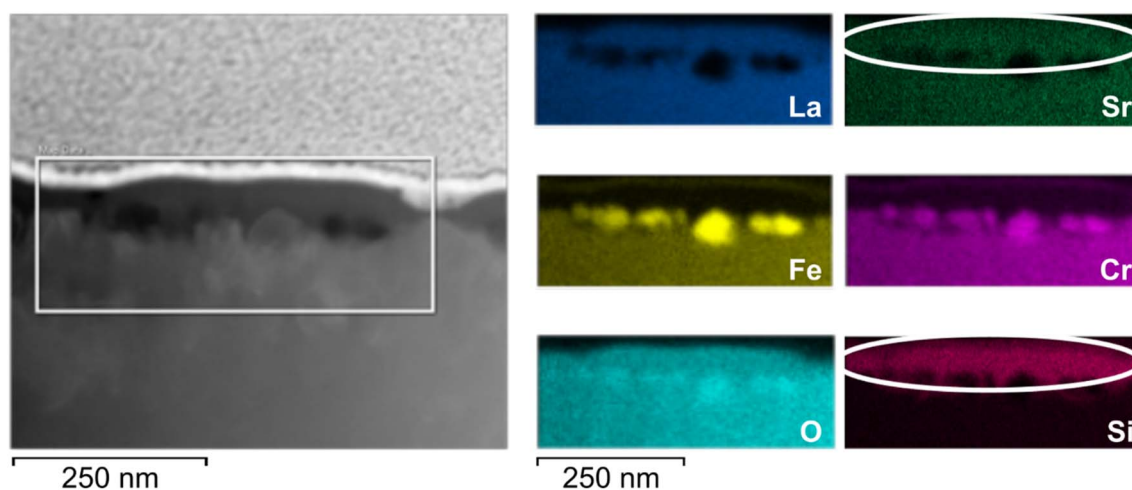

Fig. 6 STEM-EDX map focusing on the surface region of the sample annealed in water vapour at 900 °C for 27 hours highlighting the Sr- and Si-enriched top surface layer.
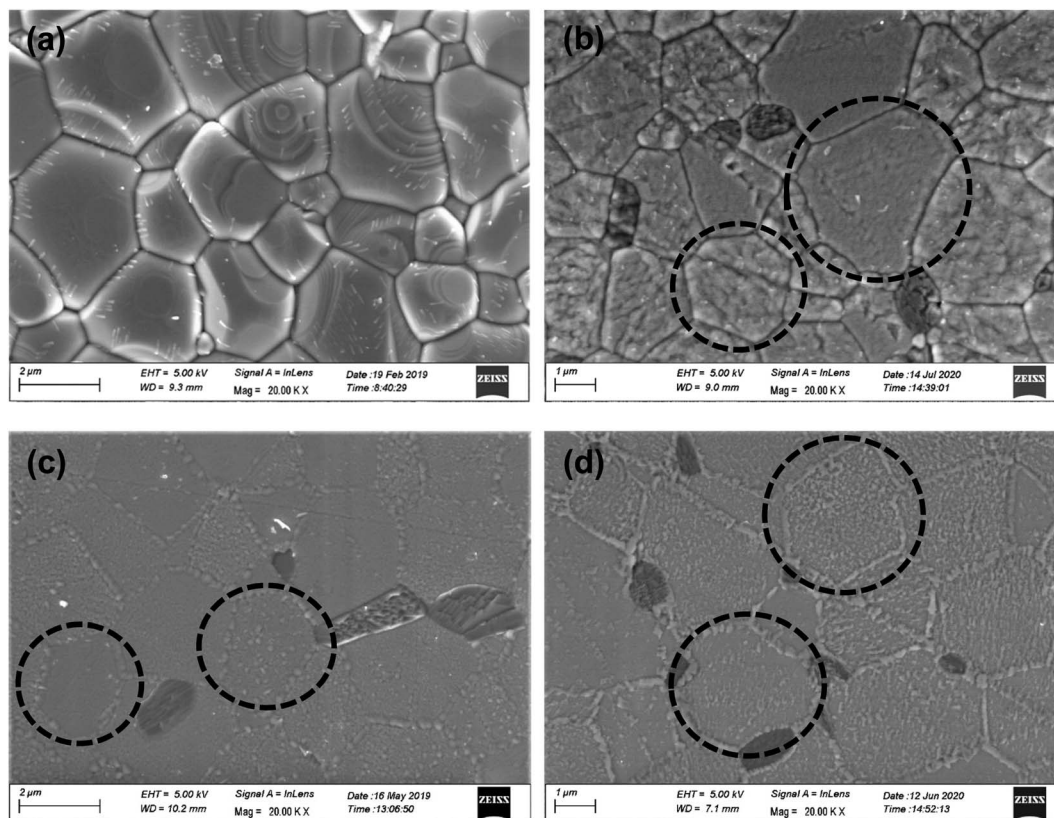
5652 | *J. Mater. Chem. A*, 2023, **11**, 5645–5659

This journal is © The Royal Society of Chemistry 2023

Fig. 7 The SE images of the (a) as sintered LSCrF8255 sample, and the sample annealed in (b) dry oxygen, (c) wet oxygen and (d) water vapour at 900 °C for 27 hours.

LSCF and $La_{0.6}Sr_{0.4}CoO_3$ under different annealing conditions.[17,23]

A phase separation also occurred on the surface of the annealed samples. Fig. S10 in the ESI† illustrates a back-scattered electron (BSE) image and SEM-EDX map collected on the sample annealed in dry oxygen at 900 °C for 27 hours. The secondary phase, which appears darker on the BSE image displayed in Fig. S10b,† was found to be significantly enriched in Fe, relatively enriched in Cr, and La and Sr deficient. The result is similar to the previous findings on the samples annealed in wet oxygen and water vapour.[24,37] Since no secondary phase was detected on the sintered sample,[24,37] the formation of the B-site cation enriched secondary phase could suggest that the material is changing from A-site deficient $A_{0.95}BO_{3-\delta}$ to an $ABO_{3-\delta}$ perovskite oxide during the annealing process under the different atmospheres.

2.2. La enriched surface chemistry

In Fig. 1c, d and Table S1,† interestingly, a La-enriched surface was observed on the samples annealed in dry oxygen at 600 and 700 °C. The atomic ratio of $[La]_{total} : [Sr]_{total}$ was found to be 89 : 11 from XPS and 87 : 13 from ARXPS at 600 °C; and 89 : 11 from XPS and 88 : 12 from ARXPS at 700 °C, higher than the stoichiometric ratio of 80 : 20. The result contrasts with the Sr-enriched surface observed and discussed previously in this work. It is common to observe an AO-terminated surface layer

on the surface of an annealed perovskite oxide,[18,30,33,42,43,48,70–74] however, a La-enriched surface is scarcely reported. An example of the La 3d spectra collected from the sample annealed in dry oxygen at 700 °C is illustrated in Fig. S11 in the ESI,† where multiplet splitting of 4.3 eV is observed. The result agrees well with the value found on the sample annealed in dry oxygen at 900 °C (Fig. 4a), suggesting that the La surface species is most likely to be La_2O_3.

LEIS sputter depth profiling was applied to verify the La-enriched surfaces found on the samples annealed in dry oxygen at intermediate temperatures. The $^{20}Ne^+$ (5 keV) LEIS spectra of the as-polished sample, and the samples annealed at 600 and 700 °C for 27 hours in dry oxygen, alongside the corresponding LEIS depth profiles of $[La]_{total} : [Sr]_{total}$ are illustrated in Fig. 8. In Fig. 8, compared to the as-polished sample, the peak intensity ratio of La to Sr is found higher in the two annealed samples. This observation contrasts with previous findings by Druce et al.,[75] where a decrease in the peak intensity ratio of La to Sr was observed in annealed LSCF samples compared to the as-polished sample. For instance, in Fig. 8b, the La peak can be clearly observed and is dominant on the outer surface of the LSCrF8255 samples annealed at 600 °C in dry oxygen, whereas only a slight trace of La was detected for the LSCF sample annealed at 600 °C in air.[75] La enrichment is also visible in the subsurface regions of the annealed samples, indicated in Fig. 8b and c. In the LEIS depth profiles in Fig. 8d,
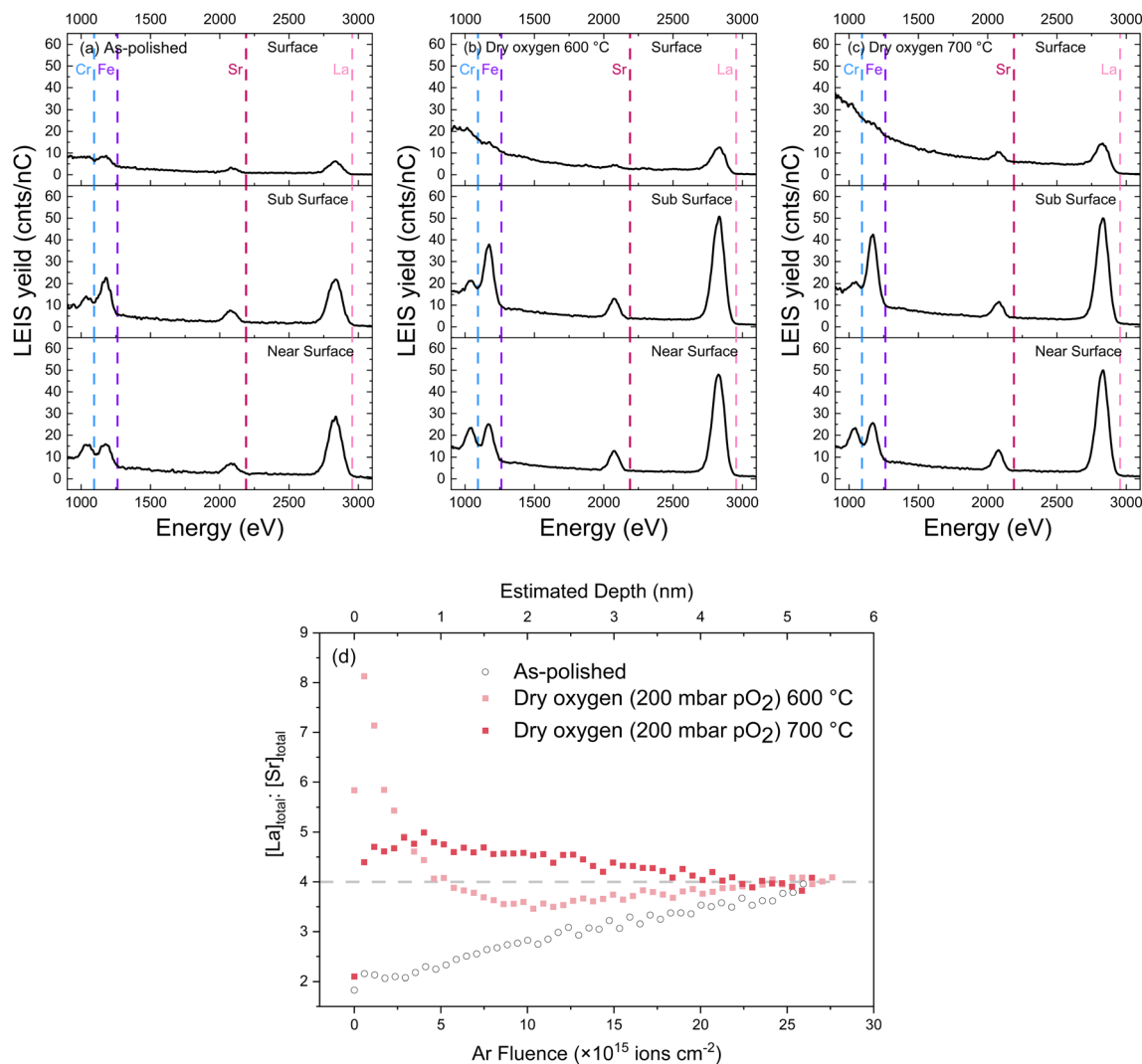
This journal is © The Royal Society of Chemistry 2023

J. Mater. Chem. A, 2023, **11**, 5645–5659 | **5653**

Fig. 8 The $^{20}Ne^+$ (5 keV) LEIS spectra of (a) the as-polished LSCrF8255 sample, and the samples annealed in dry oxygen at (b) 600 and (c) 700 °C. The top rows display the spectra obtained for immediate surfaces, the middle row are the spectra obtained for sub-surfaces after removal of a small amount of material by Ar^+ sputtering of approximately 4.6×10^{15} cm^{-2}, and the bottom row shows the spectra obtained for near surfaces after sputtering up to a fluence $>25 \times 10^{15}$ cm^{-2}; (d) LEIS depth profiles showing atomic ratio of $[La]_{total} : [Sr]_{total}$ for the as-polished LSCrF8255 sample, and the sample annealed in dry oxygen at 600 and 700 °C. The dashed line indicates the nominal bulk stoichiometry.

compared to the outermost atomic layers of the as-polished sample which are enriched in Sr, the outermost atomic layers of the samples annealed in dry oxygen at 600 and 700 °C are relatively enriched in La up to Ar^+ fluences of 25×10^{15} cm^{-2} (estimated depth ~5 nm).

The SEM micrographs and a STEM-EDX map collected from the samples annealed in dry oxygen at 600 and 700 °C are illustrated in Fig. 9.

Fig. 9 shows the formation of precipitates on the surfaces. In Fig. 9c, the surface particle on the sample annealed in dry oxygen at 600 °C was found to be relatively Sr- and Cr-enriched. This finding is consistent with the Sr- and Cr-enriched top surface layer found on the sample annealed in dry oxygen at 900 °C shown in Fig. 5. Once again, this suggests that Cr deposition on LSCrF8255 is highly selective and preferentially takes place on the SrO, forming SrCrO$_4$-like

particles. The Cr evaporation and redeposition on the surface is also supported by the XPS results. Table S6 in the ESI† presents the atomic ratios of $[Cr^{6+}] : [Cr^{3+}]$ and $[Cr]_{total} : [Fe]_{total}$ obtained from the LSCrF8255 samples annealed in dry oxygen at 600 and 700 °C through XPS (≈ 10 nm probe depth) and ARXPS (<1 nm probe depth). The Cr^{6+} content and the total Cr content are found to be higher with increasing surface sensitivity, and a small degree of Cr enrichment (by 7 at.%) is detected on the outer surface layers of the samples measured through ARXPS. It is also worth mentioning that, in addition to the surface particles, a secondary phase forms on the dry oxygen annealed samples at 600 and 700 °C. Fig. S12 in the ESI† illustrates the SEM BSE images collected on the samples, where the secondary phase appears darker. A STEM-EDX map collected on the sample annealed at 600 °C is illustrated in Fig. S13 in the ESI,† indicating the secondary phase is B-site
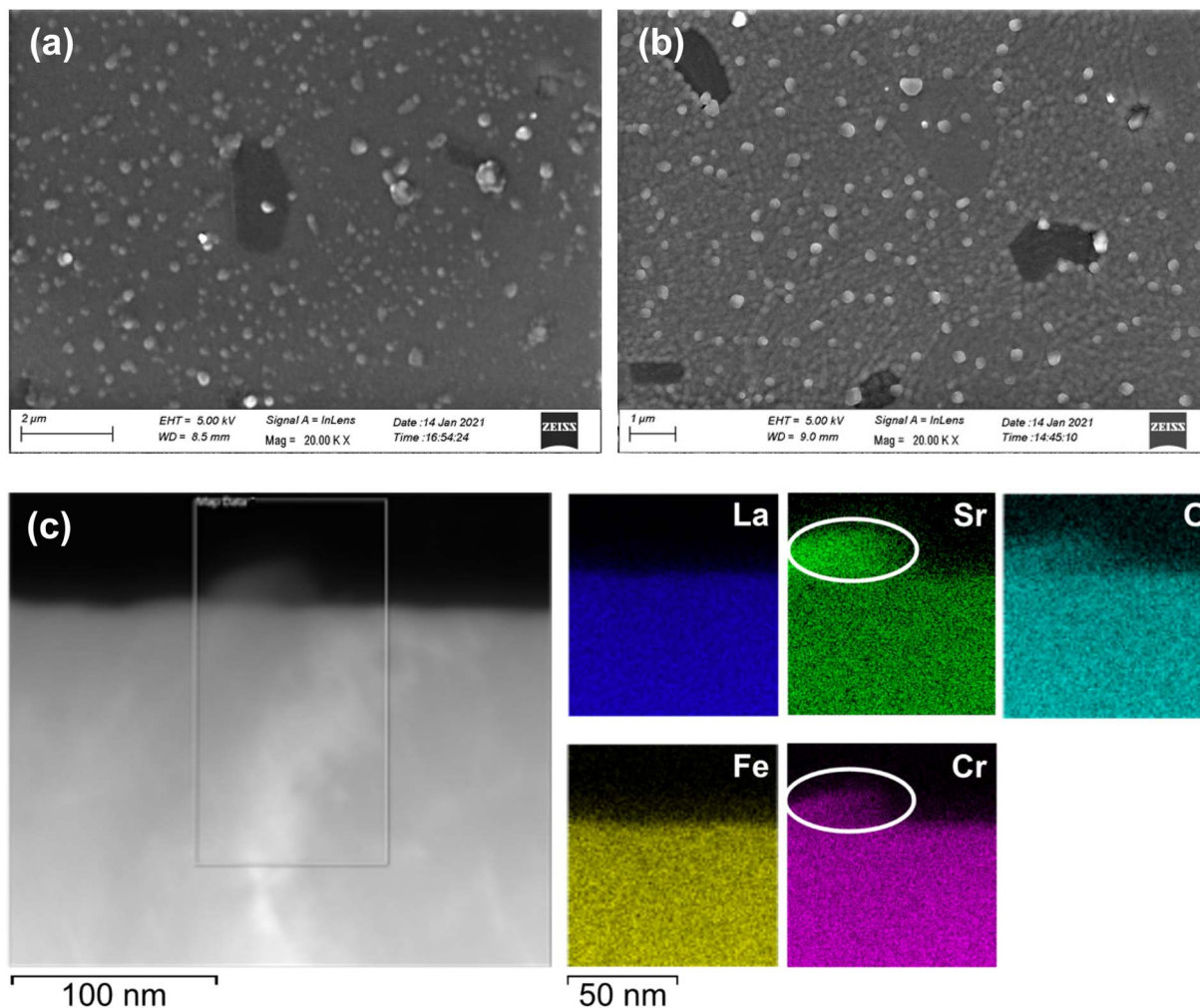
5654 | *J. Mater. Chem. A*, 2023, **11**, 5645–5659

This journal is © The Royal Society of Chemistry 2023

Fig. 9 The SEM SE images of the LSCrF8255 samples annealed in dry oxygen at (a) 600 °C and (b) 700 °C for 27 hours; (c) STEM-EDX map represents the surface region of the sample annealed in dry oxygen at 600 °C for 27 hours highlighting the Sr- and Cr-enriched surface particle.

cation (Fe and Cr) enriched and A-site cation (La and Sr) deficient. This result is in line with the previous discussion in Section 2.1.2.3.

Based on the experimental evidence, it is very likely that the La-enriched surface is the result of the potential surface evaporation process regarding Sr and Cr. To prove this, a Si wafer was placed beside the LSCrF8255 during the annealing in dry oxygen at 600 °C. In the SIMS analysis on the Si wafer, traces of La^+, Sr^+, Cr^+, and Fe^+ were found. The 3D reconstruction of the signals are illustrated in Fig. S14 in the ESI.† The intensities were estimated with the relative sensitivity factors (RSF) of elements on a Si wafer under an oxygen sputtering beam[76] and further normalized with ^{56}Fe displayed in Table S7 in the ESI.† In Table S7,† the intensities of the Sr^+ and Cr^+ signals are significantly higher than the others on the Si wafer, confirming the possibility of Sr and Cr surface evaporation.

In order to further investigate whether the phenomenon is thermodynamically or kinetically driven, a LSCrF8255 sample was annealed in dry oxygen at 600 °C for 8 days – a significantly longer period of time than the previously used 27 hours period.

Table S8 in the ESI† presents the atomic ratio of $[Sr]_{surface}$: $[Sr]_{bulk}$ and $[La]_{total}$: $[Sr]_{total}$, measured by XPS and ARXPS, from the two samples annealed in dry oxygen at 600 °C with different durations. In Table S8,† the ratios of $[Sr]_{surface}$: $[Sr]_{bulk}$ and $[La]_{total}$: $[Sr]_{total}$ are approximately constant between the two samples, suggesting a similar amount of La and Sr species on the surface. For both samples, the $[La]_{total}$: $[Sr]_{total}$ ratio is approximately 90 : 10 measured through XPS and ARXPS, indicating La-enriched surfaces. The LEIS depth profiles of the samples annealed at 600 °C for 27 hours and 8 days are illustrated in Fig. 10.

In Fig. 10, a slightly higher La enrichment level can be observed on the top surface layers of the sample annealed for 8 days up to Ar^+ fluences of 20×10^{15} cm^{-2} (estimated depth ~4 nm). This result suggests that the extent of La enrichment could increase marginally with annealing duration. Finally, it is worth noting that all the results reported in this study should represent snapshots of the dynamic surface chemistry evolution with defined annealing temperature and time.
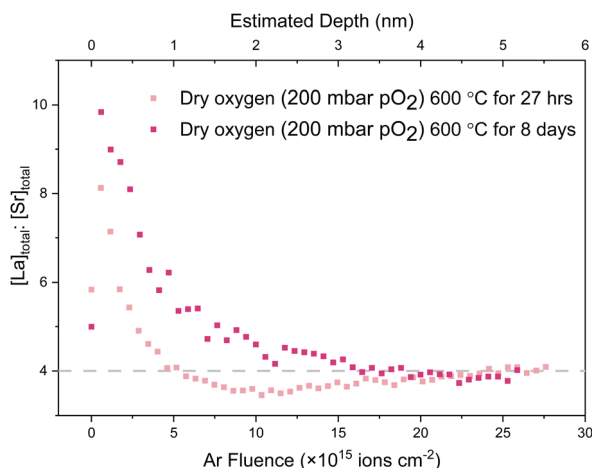
Fig. 10 LEIS depth profiles showing atomic ratio of $[La]_{total} : [Sr]_{total}$ for the LSCrF8255 samples annealed in dry oxygen at 600 °C for 27 hours and for 8 days. The dashed line indicates the bulk stoichiometry.

3 Conclusions

Using surface chemical state quantification analysis through XPS and LEIS as a guideline, combined with results from SEM, SEM-EDX, STEM-EDX, and ToF-SIMS, the surface composition and evolution of $(La_{0.8}Sr_{0.2})_{0.95}Cr_{0.5}Fe_{0.5}O_{3-\delta}$ (LSCrF8255) as a model perovskite oxide was investigated systematically under dry oxygen ($pO_2 = 200$ mbar), wet oxygen ($pO_2 = 200$ mbar, $pH_2O = 30$ mbar), and water vapour ($pO_2 < 1$ mbar, $pH_2O = 30$ mbar) environments. Sr surface segregation has been demonstrated on samples annealed in all three atmospheres at high temperatures. Comparing the samples annealed at 900 °C in dry oxygen, wet oxygen, and water vapour for 27 hours, XPS and LEIS results show that the surface of the sample annealed in water vapour displayed the highest fraction of Sr in surface species compared to Sr in the perovskite structure, however, the surface of the sample annealed in dry oxygen showed the highest overall Sr surface enrichment. Sr surface segregation and enrichment is likely suppressed on the sample annealed in wet oxygen. In addition, through analysis of the selected region at the surface of the annealed sample with SEM, SEM-EDX, and STEM-EDX, the Sr segregation behaviour has been found to correlate with Cr evaporation and redeposition and Si deposition. The Sr-enriched surface precipitate phase was likely to be $SrCrO_4$-like or a mixture of $SrCrO_4$-like and SrO_x on the sample annealed in dry oxygen, and $SrSiO_4$-like or a mixture of $SrSiO_4$-like, $Sr(OH)_2$ and SrO_x on the samples annealed in wet oxygen and water vapour. Further, the crystal orientation and defects such as grain boundaries and dislocations could also have an impact on the Sr segregation behaviour. In addition to the Sr-enriched surface precipitates, phase separation was consistently observed on all samples annealed in the three conditions. The secondary phase is B-site cation enriched (significantly Fe enriched, relatively Cr enriched) and A-site cation (La and Sr) deficient. Moreover, in contrast to the Sr enriched surface, a La enriched surface was observed on the samples annealed in dry oxygen at 600 and 700 °C. Through ToF-SIMS analysis of a Si wafer placed beside the LSCrF8255 sample during annealing, it has been concluded that the La enriched surface is very likely to be the result of Sr and Cr surface evaporation processes. Our scientific findings are expected to provide an advancement in understanding and guidelines for material design, performance, and durability of MIEC perovskite oxides in energy conversion applications such as SOFCs, SOECs, and OTMs which require oxygen reduction/evolution and H_2O electrolysis.

4 Experimental section

The $(La_{0.8}Sr_{0.2})_{0.95}Cr_{0.5}Fe_{0.5}O_{3-\delta}$ (LSCrF8255) powders were supplied by Praxair, Inc., USA (LOT: 03-P6760DM). Dense ceramic pellets (>97% of theoretical density) were prepared by sintering green pellets formed by pressing the powders uni-axially at a load of 2 tons and isostatically at a load of 300 MPa at 1450 °C for a duration of 6 hours in static laboratory air. The sintered pellets were then ground with successive grades of SiC paper (Struers Ltd, UK) and polished with water-based diamond suspensions (Struers Ltd, UK) down to 1/4 μm finish to reduce any potential error arising from surface roughness. The as-polished samples were annealed under a dry oxygen atmosphere with 200 mbar of high purity oxygen (BOC Ltd, 99.999%, corresponding to the "dry" conditions); a wet oxygen atmosphere with 200 mbar of high purity oxygen (ST Gas Ltd, 99.999%) plus 30 mbar of water vapour pressure; and a water vapour atmosphere with 30 mbar of vapour pressure and less than 1 mbar of oxygen partial pressure, each at 600–900 °C with home-built rigs.[37]

X-ray photoelectron spectroscopy (XPS) and angle-resolved XPS (ARXPS) were conducted using a high-throughput spectrometer (K-Alpha$^+$, Thermo Fisher Scientific, USA) with a monochromated Al K$_\alpha$ radiation source ($h\nu = 1486.6$ eV) operating at 2×10^{-9} mbar base pressure. The X-ray source applied a 6 mA emission current and 12 kV anode bias, giving an X-ray spot size of up to 400 μm^2. Survey and core-level spectra were collected at two sample tilt angles, 0° and 80°, with increasing sensitivity to the surface at higher tilt angles. The average probe depth is approximately 10 nm with XPS and less than 1 nm with ARXPS. The binding energies were calibrated using the C 1s peak at 284.8 eV. Spectra were processed by subtraction of a Shirley-type[44] background and peaks were fitted using a Gaussian–Lorentzian line shape.

The surface and near-surface chemical compositions were also investigated by low energy ion scattering spectroscopy (LEIS) using a Qtac^{100} spectrometer (ION-TOF GmbH, Germany). The instrument is equipped with a dual-beam system, comprising a primary analysing gun with a square beam of analysis area 1 mm × 1 mm, and a sputtering gun with a square beam sputter area of 1.5 mm × 1.5 mm. $^{20}Ne^+$ (5 keV) was used as the primary ion beam to analyse sample surfaces, and the Ar$^+$ sputtering gun at 59° incidence was used to obtain atomic composition information as a function of depth. During LEIS analysis, the projectile is perpendicularly focused on the sample surface ($\alpha = 0°$) and backscattered ions at all azimuths are collected by the toroidal energy analyser (DTA) at a scattering angle of 145°. More details regarding the LEIS data

5656 | J. Mater. Chem. A, 2023, **11**, 5645–5659

This journal is © The Royal Society of Chemistry 2023

interpretation including the fitting of the scattering peaks, and the calibration method applied to obtain the depth profiles, are introduced in Section S1 in the ESI†.

Secondary ion mass spectrometry (SIMS) analysis was performed on a time-of-flight (ToF) SIMS spectrometer (ToF-SIMS V, IONTOF GmbH, Germany). The measurements were conducted in the high current bunch mode for higher mass resolution using a Bi^+ analysis beam (25 keV) with a 100 μm × 100 μm analytical area, and a O^+ sputtering beam (1 keV) with a sputtering area of 300 μm × 300 μm. For the data analysis, the intensities of all species of interest were point-to-point normalized to the total counts. 3D reconstruction was carried out using Surfacelab 7.0 software to visualize the distribution of different species.

In addition, scanning electron microscopy (SEM) and energy-dispersive X-ray spectroscopy (EDX) in SEM mode (SEM-EDX) were carried out using the LEO Gemini 1525 field emission gun (FEG)-SEM (Carl Zeiss Ltd, Germany) microscope equipped with an INCA X-act EDX detector (Oxford Instruments Ltd, UK). The secondary electron (SE) and backscattered electron (BSE) images were collected under an accelerating voltage of 5 kV and an aperture size of 60 μm, and the SEM-EDX analysis was conducted under an accelerating voltage of 15 or 20 kV and an aperture size of 60 μm.

Further investigation into the chemical composition of phases was performed through scanning transmission electron microscopy (STEM) with the JEM-2100F TEM/STEM (JEOL Ltd, Japan) microscope operated at 200 kV and equipped with an INCA/Aztech EDX 80 mm X-Max detector system (Oxford Instruments Ltd, UK). The STEM-EDX mapping was carried out using a 0.7 nm spot size and 20 cm camera length. The thin electron-transparent lamellae for STEM analysis were prepared from LSCrF8255 pellets by gallium ion milling using a focused ion beam scanning electron microscope (FIB-SEM) (Helios NanoLab 600, Thermo Fisher Scientific, US).

Conflicts of interest

There are no conflicts to declare.

Acknowledgements

References

1 J. A. Kilner, S. J. Skinner, S. J. C. Irvine and P. P. Edwards, *Functional Materials for Sustainable Energy Applications*, Woodhead Publishing Limited, Oxford, 2012.

2 H. L. Tuller, J. Schoonman and I. Riess, *Oxygen Ion and Mixed Conductors and Their Technological Applications*, Kluwer Academic, 2000.

3 S. Gupta, M. K. Mahapatra and P. Singh, Lanthanum chromite based perovskites for oxygen transport membrane, *Mater. Sci. Eng. R Rep.*, 2015, **90**, 1–36.

4 C. Sun, J. A. Alonso and J. Bian, Recent Advances in Perovskite-Type Oxides for Energy Conversion and Storage Applications, *Adv. Energy Mater.*, 2021, **11**, 1–21.

5 L. Shu, *et al.*, Advanced perovskite anodes for solid oxide fuel cells: A review, *Int. J. Hydrogen Energy*, 2019, **44**, 31275–31304.

6 A. Jun, J. Kim, J. Shin and G. Kim, Perovskite as a Cathode Material: A Review of its Role in Solid-Oxide Fuel Cell Technology, *ChemElectroChem*, 2016, **3**, 511–530.

7 W. Li, X. Zhu, Z. Cao, W. Wang and W. Yang, Mixed ionic-electronic conducting (MIEC) membranes for hydrogen production from water splitting, *Int. J. Hydrogen Energy*, 2015, **40**, 3452–3461.

8 M. A. Laguna-Bercero, Recent advances in high temperature electrolysis using solid oxide fuel cells: A review, *J. Power Sources*, 2012, **203**, 4–16.

9 W. Jung and H. L. Tuller, Investigation of surface Sr segregation in model thin film solid oxide fuel cell perovskite electrodes, *Energy Environ. Sci.*, 2012, **5**, 5370–5378.

10 Z. Cai, M. Kubicek, J. Fleig and B. Yildiz, Chemical heterogeneities on $La_{0.6}Sr_{0.4}CoO_{3-\delta}$ thin films-correlations to cathode surface activity and stability, *Chem. Mater.*, 2012, **24**, 1116–1127.

11 W. Lee, J. W. Han, Y. Chen, Z. Cai and B. Yildiz, Cation size mismatch and charge interactions drive dopant segregation at the surfaces of manganite perovskites, *J. Am. Chem. Soc.*, 2013, **135**, 7909–7925.

12 B. Koo, *et al.*, Enhanced oxygen exchange of perovskite oxide surfaces through strain-driven chemical stabilization, *Energy Environ. Sci.*, 2018, **11**, 71–77.

13 E. Bucher and W. Sitte, Long-term stability of the oxygen exchange properties of $(La,Sr)_{1-z}(Co,Fe)O_{3-\delta}$ in dry and wet atmospheres, *Solid State Ionics*, 2011, **192**, 480–482.

14 Y. Chen, *et al.*, Impact of Sr segregation on the electronic structure and oxygen reduction activity of $SrTi_{1-x}Fe_xO_3$ surfaces, *Energy Environ. Sci.*, 2012, **5**, 7979–7988.

15 J. Choi, H. Dulli, S. H. Liou, P. A. Dowben and M. A. Langell, The influence of surface terminal layer and surface defects on the electronic structure of CMR perovskites: $La_{0.65}A_{0.35}MnO_3$ (A = Ca, Sr, Ba), *Phys. Status Solidi B Basic Res.*, 1999, **214**, 45–57.

16 B. Koo, K. Kim, J. K. Kim, H. Kwon and J. W. Han, Sr Segregation in Perovskite Oxides : Why It Happens and How It Exists, *Joule*, 2018, **2**, 1476–1499.

17 M. Niania, *et al.*, In situ study of strontium segregation in $La_{0.6}Sr_{0.4}Co_{0.2}Fe_{0.8}O_{3-\delta}$ in ambient atmospheres using high-temperature environmental scanning electron microscopy, *J. Mater. Chem. A*, 2018, **6**, 14120–14135.

This journal is © The Royal Society of Chemistry 2023

J. Mater. Chem. A, 2023, **11**, 5645–5659 | **5657**

18 J. Druce, *et al.*, Surface termination and subsurface restructuring of perovskite-based solid oxide electrode materials, *Energy Environ. Sci.*, 2014, **7**, 3593–3599.

19 S. P. Simner, M. D. Anderson, M. H. Engelhard and J. W. Stevenson, Degradation mechanisms of La-Sr-Co-Fe-O$_3$ SOFC cathodes, *Electrochem. Solid-State Lett.*, 2006, **9**, 3–7.

20 T. T. Fister, *et al.*, In situ characterization of strontium surface segregation in epitaxial La$_{0.7}$Sr$_{0.3}$MnO$_3$ thin films as a function of oxygen partial pressure, *Appl. Phys. Lett.*, 2008, **93**, 1–4.

21 H. Jalili, J. W. Han, Y. Kuru, Z. Cai and B. Yildiz, New insights into the strain coupling to surface chemistry, electronic structure, and reactivity of La$_{0.7}$Sr$_{0.3}$MnO$_3$, *J. Phys. Chem. Lett.*, 2011, **2**, 801–807.

22 N. Tsvetkov, Q. Lu, L. Sun, E. J. Crumlin and B. Yildiz, Improved chemical and electrochemical stability of perovskite oxides with less reducible cations at the surface, *Nat. Mater.*, 2016, **15**, 1010–1016.

23 F. Pişkin, R. Bliem and B. Yildiz, Effect of crystal orientation on the segregation of aliovalent dopants at the surface of La$_{0.6}$Sr$_{0.4}$CoO$_3$, *J. Mater. Chem. A*, 2018, **6**, 14136–14145.

24 Z. Sha, E. Cali, G. Kerherve and S. J. Skinner, Oxygen diffusion behaviour of A-site deficient (La$_{0.8}$Sr$_{0.2}$)$_{0.95}$Cr$_{0.5}$Fe$_{0.5}$O$_{3-δ}$ perovskites in humid conditions, *J. Mater. Chem. A*, 2020, **8**, 21273–21288.

25 Z. Cai, M. Kubicek, J. Fleig and B. Yildiz, Chemical heterogeneities on La$_{0.6}$Sr$_{0.4}$CoO$_{3-δ}$ thin films-correlations to cathode surface activity and stability, *Chem. Mater.*, 2012, **24**, 1116–1127.

26 M. Kubicek, A. Limbeck, T. Frömling, H. Hutter and J. Fleig, Relationship between Cation Segregation and the Electrochemical Oxygen Reduction Kinetics of La$_{0.6}$Sr$_{0.4}$CoO$_{3-δ}$ Thin Film Electrodes, *J. Electrochem. Soc.*, 2011, **158**, B727.

27 Z. Pan, Q. Liu, L. Zhang, X. Zhang and S. H. Chan, Effect of Sr Surface Segregation of La$_{0.6}$Sr$_{0.4}$Co$_{0.2}$Fe$_{0.8}$O$_{3-δ}$ Electrode on Its Electrochemical Performance in SOC, *J. Electrochem. Soc.*, 2015, **162**, F1316–F1323.

28 A. K. Huber, *et al.*, In situ study of activation and de-activation of LSM fuel cell cathodes - Electrochemistry and surface analysis of thin-film electrodes, *J. Catal.*, 2012, **294**, 79–88.

29 G. M. Rupp, A. K. Opitz, A. Nenning, A. Limbeck and J. Fleig, Real-time impedance monitoring of oxygen reduction during surface modification of thin film cathodes, *Nat. Mater.*, 2017, **16**, 640–645.

30 G. M. Rupp, *et al.*, Surface chemistry of La$_{0.6}$Sr$_{0.4}$CoO$_{3-δ}$ thin films and its impact on the oxygen surface exchange resistance, *J. Mater. Chem. A*, 2015, **3**, 22759–22769.

31 R. Bachelet, F. Sánchez, F. J. Palomares, C. Ocal and J. Fontcuberta, Atomically flat SrO-terminated SrTiO$_3$ (001) substrate, *Appl. Phys. Lett.*, 2009, **95**, 10–13.

32 A. Staykov, *et al.*, Interaction of SrO-terminated SrTiO$_3$ surface with oxygen, carbon dioxide, and water, *J. Mater. Chem. A*, 2018, **6**, 22662–22672.

33 A. Staykov, *et al.*, Oxygen Activation and Dissociation on Transition Metal Free Perovskite Surfaces, *Chem. Mater.*, 2015, **27**, 8273–8281.

34 M. P. De Jong, V. A. Dediu, C. Taliani and W. R. Salaneck, Electronic structure of La$_{0.7}$Sr$_{0.3}$MnO$_3$ thin films for hybrid organic/inorganic spintronics applications, *J. Appl. Phys.*, 2003, **94**, 7292–7296.

35 E. Mutoro, E. J. Crumlin, M. D. Biegalski, H. M. Christen and Y. Shao-Horn, Enhanced oxygen reduction activity on surface-decorated perovskite thin films for solid oxide fuel cells, *Energy Environ. Sci.*, 2011, **4**, 3689–3696.

36 S. F. Wagner, *et al.*, Enhancement of oxygen surface kinetics of SrTiO$_3$ by alkaline earth metal oxides, *Solid State Ionics*, 2006, **177**, 1607–1612.

37 Z. Sha, *et al.*, Significantly Enhanced Oxygen Transport Properties in Mixed Conducting Perovskite Oxides under Humid Reducing Environments, *Chem. Mater.*, 2021, **33**, 8469–8476.

38 D. Chen, *et al.*, Revising the role of chromium on the surface of perovskite electrodes: Poison or promoter for the solid oxide electrolysis cell performance?, *J. Catal.*, 2020, **381**, 520–529.

39 D. Kim, R. Bliem, F. Hess, J. J. Gallet and B. Yildiz, Electrochemical Polarization Dependence of the Elastic and Electrostatic Driving Forces to Aliovalent Dopant Segregation on LaMnO$_3$, *J. Am. Chem. Soc.*, 2020, **142**, 3548–3563.

40 E. Ostrovskiy, Y. L. Huang and E. D. Wachsman, Effects of surface chemical potentials on cation segregation, *J. Mater. Chem. A*, 2021, **9**, 1593–1602.

41 J. A. Kilner, H. Tellez Lozano, M. Burriel, S. Cook and J. Druce, The Application of Ion Beam Analysis to Mass Transport Studies in Mixed Electronic Ionic Conducting Electrodes, *ECS Trans.*, 2013, **57**, 1701–1708.

42 H. Téllez, *et al.*, New perspectives in the surface analysis of energy materials by combined time-of-flight secondary ion mass spectrometry (ToF-SIMS) and high sensitivity low-energy ion scattering (HS-LEIS), *J. Anal. At. Spectrom.*, 2014, **29**, 1361–1370.

43 Y. Moryson, *et al.*, Analyzing Nanometer-Thin Cathode Particle Coatings for Lithium-Ion Batteries—The Example of TiO$_2$ on NCM622, *ACS Appl. Energy Mater.*, 2021, **4**, 7168–7181.

44 D. A. Shirley, High-resolution x-ray photoemission spectrum of the valence bands of gold, *Phys. Rev. B*, 1972, **5**, 4709–4714.

45 C. H. Wong, Effect of Aging on ScSZ/LSCrF Dual-Phase Oxygen Transport Membrane for Syngas Production, PhD thesis, Imperial College London, 2017.

46 M. Siebenhofer, *et al.*, Surface Chemistry and Degradation Processes of Dense La$_{0.6}$Sr$_{0.4}$CoO$_{3-δ}$ Thin Film Electrodes, *J. Electrochem. Soc.*, 2023, **170**, 014501.

47 V. Thoréton, M. Niania and J. Kilner, Kinetics of competing exchange of oxygen and water at the surface of functional oxides, *Phys. Chem. Chem. Phys.*, 2021, **23**, 2805–2811.

48 M. Niania, M. Sharpe, R. Webb and J. A. Kilner, The surface of complex oxides; ion beam based analysis of energy

5658 | *J. Mater. Chem. A*, 2023, **11**, 5645–5659

This journal is © The Royal Society of Chemistry 2023

materials, *Nucl. Instrum. Methods Phys. Res., Sect. B*, 2020, **480**, 27–32.

49 M. P. Seah, The quantitative analysis of surfaces by XPS: A review, *Surf. Interface Anal.*, 1980, **2**, 222–239.

50 M. F. Sunding, *et al.*, XPS characterisation of *in situ* treated lanthanum oxide and hydroxide using tailored charge referencing and peak fitting procedures, *J. Electron Spectrosc. Relat. Phenom.*, 2011, **184**, 399–409.

51 P. A. W. Van Der Heide, Systematic x-ray photoelectron spectroscopic study of $La_{1-x}Sr_x$-based perovskite-type oxides, *Surf. Interface Anal.*, 2002, **33**, 414–425.

52 W. Y. Howng and R. J. Thorn, Investigation of the electronic structure of $La_{1-x}(M^{2+})_xCrO_3$, Cr_2O_3 and La_2O_3 by X-ray photoelectron spectroscopy, *J. Phys. Chem. Solids*, 1980, **41**, 75–81.

53 Y. Uwamino, T. Ishizuka and H. Yamatera, X-ray photoelectron compounds spectroscopy of rare-earth, *J. Electron Spectrosc. Relat. Phenom.*, 1984, **34**, 67–78.

54 K. Tabata, I. Matsumoto and S. Kohiki, Surface characterization and catalytic properties of La_{1-x}-Sr_xCoO_3, *J. Mater. Sci.*, 1987, **22**, 1882–1886.

55 N. Gunasekaran, Surface characterization and catalytic properties of perovskite type solid oxide solutions, $La_{0.8}Sr_{0.2}BO_3$ (B = Cr, Mn, Fe, Co or Y), *Solid State Ionics*, 1996, **83**, 145–150.

56 H. Wei, *et al.*, Study of SrO segregation on $SrTiO_3$ (100) Surfaces, *J. Eur. Ceram. Soc.*, 2001, **21**, 1677–1680.

57 L. Qiao, *et al.*, The impact of crystal symmetry on the electronic structure and functional properties of complex lanthanum chromium oxides, *J. Mater. Chem. C*, 2013, **1**, 4527–4535.

58 E. Ünveren, E. Kemnitz, S. Hutton, A. Lippitz and W. E. S. Unger, Analysis of highly resolved x-ray photoelectron Cr 2p spectra obtained with a Cr_2O_3 powder sample prepared with adhesive tape, *Surf. Interface Anal.*, 2004, **36**, 92–95.

59 M. C. Biesinger, C. Brown, J. R. Mycroft, R. D. Davidson and N. S. McIntyre, X-ray photoelectron spectroscopy studies of chromium compounds, *Surf. Interface Anal.*, 2004, **36**, 1550–1563.

60 M. C. Biesinger, *et al.*, Resolving surface chemical states in XPS analysis of first row transition metals, oxides and hydroxides: Cr, Mn, Fe, Co and Ni, *Appl. Surf. Sci.*, 2011, **257**, 2717–2730.

61 P. Mills and J. L. Sullivan, A study of the core level electrons in iron and its three oxides by means of X-ray photoelectron spectroscopy, *J. Phys. D: Appl. Phys.*, 1983, **16**, 723–732.

62 T. C. Lin, G. Seshadri and J. A. Kelber, A consistent method for quantitative XPS peak analysis of thin oxide films on clean polycrystalline iron surfaces, *Appl. Surf. Sci.*, 1997, **119**, 83–92.

63 S. P. Jiang and Y. Zhen, Mechanism of Cr deposition and its application in the development of Cr-tolerant cathodes of solid oxide fuel cells, *Solid State Ionics*, 2008, **179**, 1459–1464.

64 K. Chen, N. Ai, K. M. O'Donnell and S. P. Jiang, Highly chromium contaminant tolerant BaO infiltrated $La_{0.6}Sr_{0.4}Co_{0.2}Fe_{0.8}O_{3-\delta}$ cathodes for solid oxide fuel cells, *Phys. Chem. Chem. Phys.*, 2015, **17**, 4870–4874.

65 S. P. Jiang, S. Zhang and Y. D. Zhen, Deposition of Cr Species at (La,Sr)(Co,Fe)O₃ Cathodes of Solid Oxide Fuel Cells, *J. Electrochem. Soc.*, 2006, **153**, A127.

66 L. Zhao, J. Drennan, C. Kong, S. Amarasinghe and S. P. Jiang, Insight into surface segregation and chromium deposition on $La_{0.6}Sr_{0.4}Co_{0.2}Fe_{0.8}O_{3-\delta}$ cathodes of solid oxide fuel cells, *J. Mater. Chem. A*, 2014, **2**, 11114–11123.

67 N. Ni, C. C. Wang, S. P. Jiang and S. J. Skinner, Synergistic effects of temperature and polarization on Cr poisoning of $La_{0.6}Sr_{0.4}Co_{0.2}Fe_{0.8}O_{3-\delta}$ solid oxide fuel cell cathodes, *J. Mater. Chem. A*, 2019, **7**, 9253–9262.

68 S. P. Jiang, J. P. Zhang and X. G. Zheng, A comparative investigation of chromium deposition at air electrodes of solid oxide fuel cells, *J. Eur. Ceram. Soc.*, 2002, **22**, 361–373.

69 S. P. Jiang and X. Chen, Chromium deposition and poisoning of cathodes of solid oxide fuel cells - A review, *Int. J. Hydrogen Energy*, 2014, **39**, 505–531.

70 H. Téllez, J. Druce, J. A. Kilner and T. Ishihara, Relating surface chemistry and oxygen surface exchange in $LnBaCo_2O_{5+\delta}$ air electrodes, *Faraday Discuss.*, 2015, **182**, 145–157.

71 J. A. Kilner, H. Tellez Lozano, M. Burriel, S. Cook and J. Druce, The Application of Ion Beam Analysis to Mass Transport Studies in Mixed Electronic Ionic Conducting Electrodes, *ECS Trans.*, 2013, **57**, 1701–1708.

72 T. Akbay, *et al.*, The interaction of molecular oxygen on Lao terminated surfaces of La_2NiO_4, *J. Mater. Chem. A*, 2016, **4**, 13113–13124.

73 H. Téllez, J. Druce, Y. W. Ju, J. Kilner and T. Ishihara, Surface chemistry evolution in $LnBaCo_2O_{5+\delta}$ double perovskites for oxygen electrodes, *Int. J. Hydrogen Energy*, 2014, **39**, 20856–20863.

74 M. A. R. Niania, A. K. Rossall, J. A. van den Berg and J. A. Kilner, The effect of sub-surface strontium depletion on oxygen diffusion in $La_{0.6}Sr_{0.4}Co_{0.2}Fe_{0.8}O_{3-\delta}$, *J. Mater. Chem. A*, 2020, **8**, 19414–19424.

75 J. Druce, T. Ishihara and J. Kilner, Surface composition of perovskite-type materials studied by Low Energy Ion Scattering (LEIS), *Solid State Ionics*, 2014, **262**, 893–896.

76 R. G. Wilson, F. A. Stevie and C. W. Magee, Secondary ion mass spectrometry: a practical handbook for depth profiling and bulk impurity analysis, *Anal. Chim. Acta*, 1991, **242**, 301.

This journal is © The Royal Society of Chemistry 2023

J. Mater. Chem. A, 2023, **11**, 5645–5659 | **5659**